Spatiotemporal Reconstruction of Antarctic Near-Surface Air Temperature from MODIS Observations

Xueying Zhang,[a] Xu Dong,[a] Jing Zeng,[a,d] Shugui Hou,[b] Paul C. J. P. Smeets,[c]
Carleen H. Reijmer,[c] and Yetang Wang[a]

[a] *College of Geography and Environment, Shandong Normal University, Jinan, China*
[b] *School of Oceanography, Shanghai Jiao Tong University, Shanghai, China*
[c] *Institute for Marine and Atmospheric Research Utrecht, Utrecht University, Utrecht, Netherlands*
[d] *Shandong Institute for Food and Drug Control, Jinan, China*

ABSTRACT: MODIS (Moderate Resolution Imaging Spectroradiometer) land surface temperature measurements in combination with in situ air temperature records from 119 meteorological stations are used to reconstruct a monthly near-surface air temperature product over the Antarctic Ice Sheet (AIS) by means of a neural network model. The product is generated on a regular grid of $0.05° \times 0.05°$, spanning from 2001 to 2018. Comparison with independent in situ air temperature measurements shows low uncertainty, with a mean bias of 0.09°C, a mean absolute error of 2.23°C, and a correlation coefficient of 97%. Furthermore, the performance of the reconstruction is better than ERA5 (the fifth-generation ECMWF reanalysis model) against in situ measurements. For the 2001–18 period, the MODIS-based near-surface air temperature product yields annual warming in the East Antarctica, but cooling in the Antarctic Peninsula and West Antarctica. However, they are not statistically significant. This product can also be used to investigate the impact of the Southern Hemisphere annual mode (SAM) on year-to-year variability of air temperature. The enhanced positive phase of SAM in recent decades in austral summer has a cooling effect on East and West Antarctica. In addition, the dataset has the potential application for climate model validation and data assimilation due to the independence of the input of a numerical weather prediction model.

KEYWORDS: Atmosphere; Antarctica; Neural networks

1. Introduction

As a central component of the cryosphere, the Antarctic Ice Sheet (AIS) plays a very important role in the global climate system. Near-surface air temperature is one of the most fundamental factors in the Antarctic system, and its variations affect not only the mass variations of the ice sheet itself, but also the ecological environment, biochemical processes, and species diversity of the surrounding sea areas (Herbei et al. 2016; Convey et al. 2018). For example, the increased air temperature is an important direct or indirect contributor of the current AIS mass loss, which is likely to be doubled by 2050 (Trusel et al. 2015). Seven of 12 ice shelves around the Antarctic Peninsula significantly retreated, and even almost completely disappeared in recent decades due to climate warming. Since the 1960s, the habitat area and coverage of two Antarctic native vascular plant species (*Deschampsia antarctica* and *Colobanthus quitensis*) increased significantly (Cannone et al. 2016). Thus, it is greatly essential to quantify the changes of near-surface air temperature in Antarctica.

From the 1957/58 International Geophysical Year (IGY), a lot of efforts have been put into direct meteorological observations across the Antarctic continent. Until now, 17 manned weather stations have continuous meteorological records from the 1957/58 IGY onward. However, most of the stations are located at the edge of the ice sheet, with only two stations in the interior. As a result, it is challenging to represent climate information of the vast Antarctic interior well by relying only on the existing stations. To address this, more than 100 automatic weather stations (AWSs) have been installed on the Antarctic continent since the 1980s (Lazzara et al. 2012), and their observations provide an important supplement for Antarctic climatic research (Costanza et al. 2016). However, the extremely harsh environment (e.g., extreme temperatures and winds) in Antarctica usually results in intermittent gaps of AWS measurements, and hence long-term records are also scarce. Moreover, most of the AIS is still undocumented by AWS observations. Thus, sparseness of observed data is a primary challenge when investigating spatial and variability of temperature over the AIS.

Although significant progress has been made to improve climate models including atmospheric general circulation models (AGCMs) (Genthon and Krinner 2001; Xin et al. 2019; Liang et al. 2021) and limited area models (LAMs) for polar regions, such as the RACMO (Regional Atmospheric Climate Model) (van Lipzig et al. 2004a,b; Noël et al. 2018), MAR (Modèle Atmosphérique Régional) (Gallée and Gorodetskaya 2010), and Polar WRF (Weather Research and Forecasting) models (Guo et al. 2003; Tastula and Vihma 2011; Tastula et al. 2012), AGCMs do not adequately represent the effect of topography on air temperature due to their coarse resolution, and the LAMs suffer from the lack of high-quality forcing data at their boundaries, leading to relatively high uncertainties of the simulations (Deb et al. 2016; Zhang et al. 2022). Global reanalysis products such as ERA-Interim (the ECMWF interim reanalysis) and ERA5 are regarded as the potential resources for representing climate changes in recent decades, due to the assimilation of in situ observations. However, they often suffer from spurious

trends in the high southern latitudes (e.g., Nicolas and Bromwich 2014; Huai et al. 2019; Wang et al. 2020).

Thanks to the rapid development of satellite remote sensing technology, thermal infrared remote sensing images, which can provide spatially continuous data at a high resolution, have become an important tool to determine global surface skin temperatures. The resulting land surface temperature (LST) products were used as a substitute for near-surface air temperature or in combination with limited air temperature measurements to fill the gaps of low spatial density of weather stations when performing a comprehensive spatial and temporal analysis (Comiso 2000; Kwok and Comiso 2002; Schneider et al. 2004; Monaghan et al. 2008; Nielsen-Englyst et al. 2019). For example, the National Oceanic and Atmospheric Administration (NOAA) AVHRR satellite retrievals of surface temperature have been used as a background field for the reconstruction of AIS near-surface temperature changes over the past 50 years (Steig et al. 2009). The Moderate Resolution Imaging Spectroradiometer (MODIS) onboard the *Terra* and *Aqua* satellites provides both daytime and nighttime LST data at a relative fine resolution (~1 km). However, satellite-retrieved LST are not identical to, and even substantially different from, air temperature measurements, and thus robust estimates of air temperature derived from LST are required. As a consequence, many attempts have been made to utilize the retrievals of MODIS LST to derive air temperature by various approaches at regional scale (e.g., Mostovoy et al. 2006; Neteler 2010; Vancutsem et al. 2010; Benali et al. 2012; Kilibarda et al. 2014; Hooker et al. 2018; Zhang et al. 2018). Recently, a global monthly 2-m air temperature dataset was generated based on MODIS LST and 3253 station observations from the Global Historical Climatology Network–Monthly (GHCN-M) dataset using the geographically weighted regression (Hooker et al. 2018). However, the AIS is not included due to the data missing of the GHCN-M dataset over Antarctica.

Our objective is to reconstruct a monthly near-surface air temperature dataset over the entire grounded AIS from 2001 to 2018, using MODIS LST products in combination with air temperature records from 119 meteorological stations. The resulting air temperature variability is also examined. In addition, the dataset serves to investigate the influence of the Southern Hemisphere annual mode (SAM) on the AIS temperature changes.

2. Data and methods

a. Data

1) IN SITU OBSERVATIONS

We compiled a dataset of the quality-controlled monthly means of in situ near-surface temperature observations from the READER (Reference Antarctic Data for Environmental Research) of the Scientific Committee on Antarctic Research (Turner et al. 2004), the Antarctic Meteorological Research Center (AMRC) at the University of Wisconsin (Lazzara et al. 2012), the Italian National Antarctic Research Programme, the Australian Antarctic AWS dataset, and the IMAU (Institute for Marine
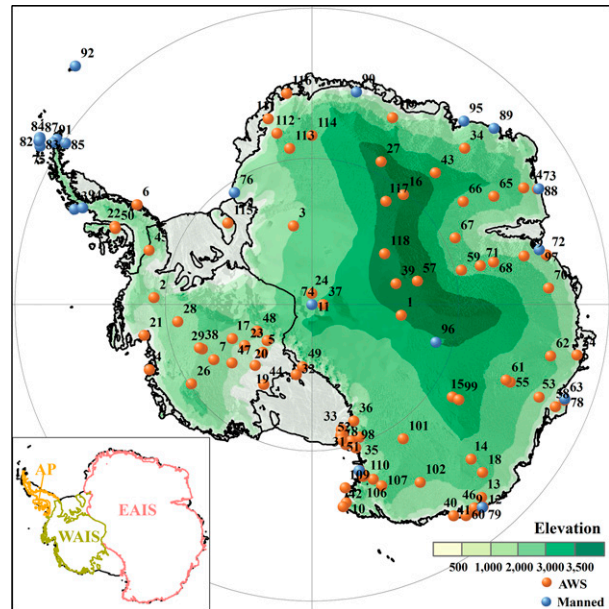

FIG. 1. Spatial distribution of 119 weather stations; station names can be found in Table A1 of appendix A.

and Atmospheric Research, Utrecht University) Antarctic AWS Project. This compilation contains near-surface air temperature observations from 119 Antarctic weather stations (95 AWSs and 24 manned stations). Their spatial distribution is shown in Fig. 1, and the corresponding coordinates, elevations, and data availability of these stations are summarized in Table A1 of appendix A.

2) MODIS SURFACE TEMPERATURE DATA

The MODIS LST data used in this paper are the monthly average LST datasets MODIS Level 3 data products MOD11C3v006 and MYD11C3v006, which are synthesized by the NASA MODIS Data Working Group after a series of preprocessing such as geometric correction and atmospheric radiation correction based on the processing of the *Terra* and *Aqua* global daily LST datasets. The datasets include daytime (LST_Day_CMG) and nighttime (LST_Night_CMG) monthly average LST data (Wan 2013), with a spatial resolution of $0.05° \times 0.05°$ (about 5.6 km at the equator). Here, we utilize MOD11C3v006 data from January 2001 to December 2018, and MYD11C3v006 between July 2002 and December 2018. By means of a radiance-based method, the mean error of the daily LST of MODIS V6 Level 2 (L2) products was estimated to be within $±0.6°C$ in 10 validation datasets, and 0.8° and 1.9°C in another two datasets, respectively (Wan 2014). For Antarctica, Fréville et al. (2014) estimated the accuracy of daily MODIS V5 LST by seven weather stations. The resulting mean biases range from $−1.8°$ to 0.1°C, and in particular, the root-mean-square errors are between 2.2° and 4.8°C at five stations on the Antarctic plateau. Because of much higher accuracy of V6 LST than V5 LST (Wan 2014), we think that MODIS V6 LST can be used as an input for the reconstruction of gridded air temperature over the AIS.

b. Methods

1) DATA PREPROCESSING

Due to the interference of cloud and other factors, the quality of each pixel of MODIS products is not always reliable. Thus, the pixel-by-pixel quality control of the MODIS LST data product is required before application. Here we use Quality Control Scientific Datasets (QC SDS) in MOD11C3 product, which provides the quality about algorithm results (LST values) of each pixel. The grid cells with "good quality" or "fairly calibrated" in the surface temperature QC_Day layer and QC_Night layer are extracted in the form of masks, and then the masks are used to screen out LST pixels. Additionally, a 15-day threshold is used as the minimum number of clear-sky days and nights available for per month, based on the Clear_sky field provided by the MOD11C3 product. Finally, the averaged values of the daytime and nighttime products are calculated for both *Terra* and *Aqua* satellites.

2) NEURAL NETWORK FITTING MODEL

The concept of neural network model originates from the neural network computational model created by McCulloch and Pitts in the 1940s, which is designed to process data by simulating the functions of the biological nervous system (McCulloch and Pitts 1943). A complete neural network model consists of several neurons in the input layer, hidden layer, and output layer. The neurons in each layer are connected by weight. Compared with other machine learning methods, the neural network model is based on statistical and mathematical models, and has more advantages in estimating and predicting sample data (Ruiz et al. 2016; Araújo et al. 2017; Sánchez et al. 2017).

A three-layer neural network fitting model is constructed to reconstruct the near-surface temperature field of the Antarctica by using the temperature data from 119 meteorological stations and the corresponding grid data from the MODIS dataset. This method uses these station values as anchoring points, and the objective of the resulting reconstructions is very close to them. According to the input, output, and complexity of the research problem, we determine the number of neurons in the input, hidden, and output layers of 1, 10, and 1, respectively. First, nearest neighbor interpolation is used to extract the preprocessed MODIS LST at the corresponding station locations. The MODIS LST values are matched with the corresponding station records. Then, the monthly near-surface air temperature of stations and the corresponding MODIS LST are respectively formed into a long time series of sample set. To improve the computing speed, the data are normalized. The sample dataset is randomly divided into training data and testing data in a ratio of 2 to 3 by stratified random samplings with respect to the stations. For model training, a subset of 40% of the data is used, and the remaining 60% are used as the test subset to assess the model performance. Training data are presented to the network during training, and the network is adjusted according to its error. Testing data are not involved into network fitting and thus provide an independent estimation of network performance during and after training (Coulibaly et al. 2000).

During the construction of neural network fitting model, 40% MODIS LST randomly screened is taken as the input of the model to establish the quantitative relationship between the station air temperature and MODIS LST in each month. The input layer integrates and passes information to the hidden layer; each neuron in the hidden layer summarizes the information of the previous layer and transfers it to the output layer through nonlinear activation function. The neuron in the output layer will process the received value into near-surface air temperature. The output results are fitted and compared with the near-surface air temperature of stations in the training data to obtain the correlation coefficients and the corresponding errors. To improve the accuracy of the model, multiple neural network learning is needed. The initial weight is randomly selected, the number of iterations is set to 1000, the predetermined target error of the neural network is 0.01, and the learning rate is 0.01. Using the error back propagation method, the error in the network training process is fed back to the neural network. The threshold and weight of the network are constantly adjusted, until the error meets the requirements or reaches the number of iterations to achieve the optimal fitting effect (here monthly R of higher than 0.95, and the mean bias values ranging from $-0.49°$ to $0.99°$C), so as to construct the monthly optimal neural network fitting model. After finishing the neural network training process, the remaining 60% observations are used to verify the reliability of the established quantitative statistical relationship between monthly station air temperature and MODIS LST. Finally, the spatiotemporally continuous MODIS LST in each month is used as the input of the trained model to generate the final reconstructed results for each month. Figure 2 shows the process of Antarctic near-surface air temperature reconstruction based on the neural network fitting model. More technical descriptions can be seen in appendix B.

3) ACCURACY ESTIMATION

Three metrics, the coefficient of determination (R^2), mean bias (MB), and mean absolute error (MAE), are used to evaluate the prediction accuracy of the neural network model; additionally, R^2 is used to reflect the degree of fitting between the predicted and observed values. MB reflects the mean difference between the two datasets. MAE can avoid the offset of positive and negative errors, and reflect the magnitude of errors between two sets of data, which is used to quantify the degree of deviation and dispersion of the predicted value relative to the actual value. Smaller values of MB and MAE mean higher accuracy of the model. The formulas for these three evaluation methods are as follows:

$$R^2 = 1 - \sum_{j}^{m} \frac{\sum_{i=1}^{n}(y_{i,j} - p_{i,j})^2}{\sum_{i=1}^{n}(y_{ij} - \bar{y})^2}, \tag{1}$$

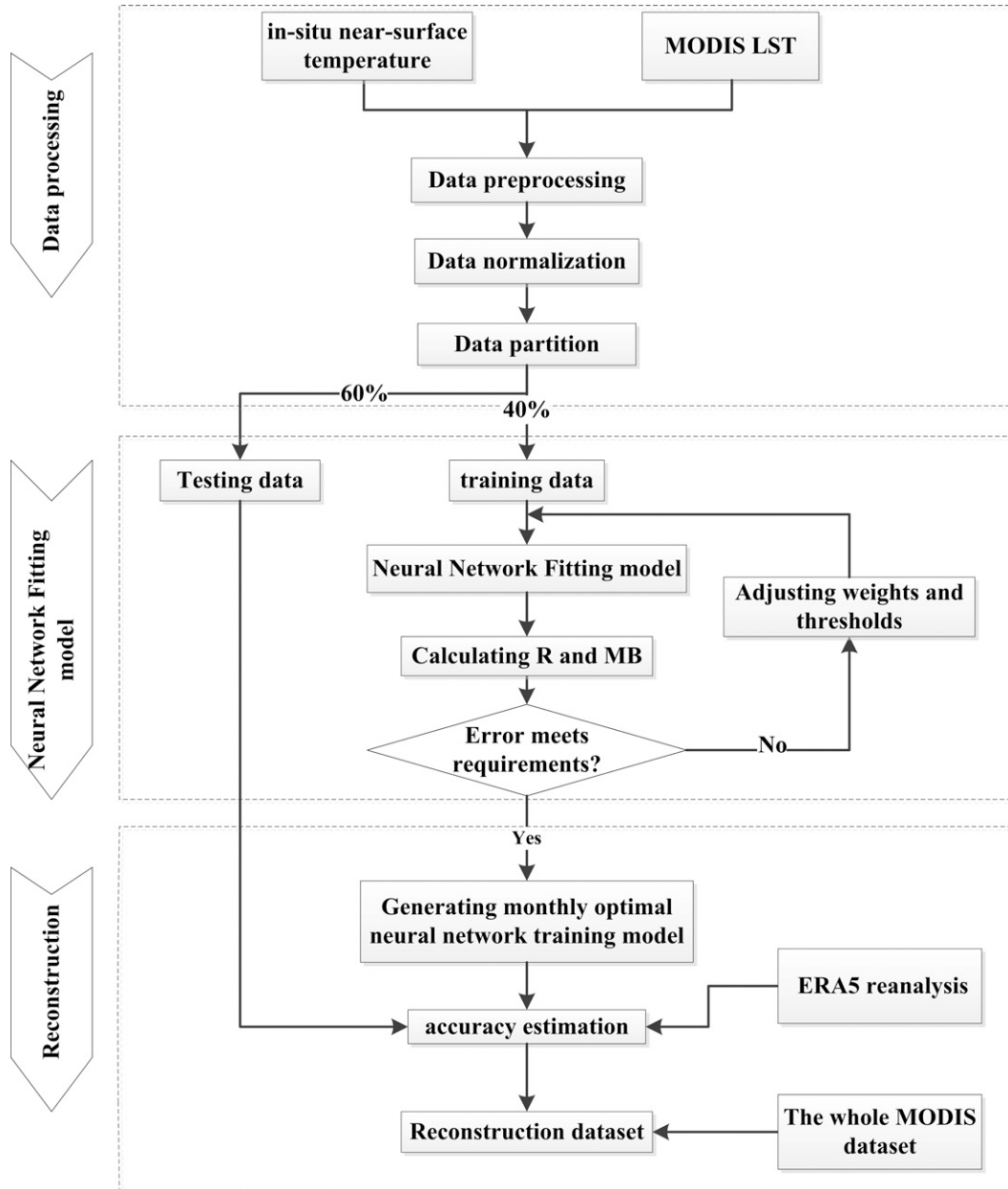$$MB = \sum_{j}^{m} \frac{\sum_{i=1}^{n}(y_{i,j} - p_{i,j})}{n}, \tag{2}$$

FIG. 2. The reconstruction process of Antarctic near-surface air temperature based on the neural network fitting model.

$$\text{MAE} = \sum_{j}^{m} \frac{\sum_{i=1}^{n} |y_{i,j} - p_{i,j}|}{n}, \qquad (3)$$

where i is the spatial index (station number) and j is the temporal index (month number). When calculating the monthly performance, $m = j$, and when calculating the overall performance, $m = 12$. Also, $y_{i,j}$ and $p_{i,j}$ are the measured and reconstructed/ERA5 values of near-surface air temperature at the meteorological stations in different months, respectively; $\bar{y}$ is the average value of measured near-surface temperature over time, and n is the number of statistical samples.

Given the complexity of the underlying Antarctic surface, nearest neighbor interpolation is adopted to extract the MODIS, ERA5, and reconstruction data at the corresponding station locations.

3. Results

a. Uncertainties of AIS near-surface temperature reconstruction

The neural network model is constructed by using the training data, and the accuracy of the model prediction is validated against the testing data [i.e., the independent in situ data as

TABLE 1. Overall performance of the satellite-derived air temperature dataset (Reconstruction) and ERA5 by comparing with independent data.

	R^2	MB (°C)	MAE (°C)
Recon	0.97	0.09	2.23
ERA5	0.96	−0.30	2.25

TABLE 2. Performance of the satellite-derived air temperature dataset (Recon) and ERA5 by comparing with independent data at each month.

Months	R^2		MB (°C)		MAE (°C)	
	Recon	ERA5	Recon	ERA5	Recon	ERA5
January	0.94	0.94	0.13	−1.14	2.01	2.01
February	0.96	0.97	0.20	−0.67	1.97	1.75
March	0.97	0.97	0.04	−0.31	2.13	2.23
April	0.97	0.96	−0.11	−0.15	2.34	2.61
May	0.97	0.96	0.13	0.11	2.16	2.54
June	0.97	0.96	−0.03	0.13	2.35	2.63
July	0.96	0.96	−0.19	0.21	2.27	2.52
August	0.97	0.97	0.08	0.37	2.30	2.58
September	0.98	0.97	0.25	0.17	2.07	2.19
October	0.96	0.97	0.22	−0.33	2.36	1.99
November	0.93	0.95	0.32	−0.83	2.45	1.87
December	0.90	0.92	0.01	−1.14	2.34	2.14

described in section 2b(1)]. The overall performance of the model is shown in Table 1. The reconstructed air temperature exhibits slightly warm bias (0.09°C), relative to the independent in situ air temperature measurements. High and significant correlation is found with R^2 of 0.97 and the MAE is estimated to be about 2.23°C.

Table 2 indicates the seasonal cycle of reliability of the satellite-derived air temperature dataset. For any month, the R^2 exceeds 0.90. Cold biases occur in April, June, and July, whereas warm biases are observed for the other months. MAE shows the dependence of seasonality, with the minimum value (1.97°C) in summer months. Seasonal dependence of the performance for air temperature over the AIS is found in the reanalysis products such as CFSR, ERA-Interim, MERRA-2, and so on over the AIS (Huai et al. 2019). ERA5 also exhibits better quality over the summer, whereas relatively poor performance occurs in winter (Table 2).

b. Comparison with ERA5 reanalysis

To further verify the reliability of the MODIS-derived near-surface temperature dataset, we compare its performance with ERA5 global reanalysis for 2-m air temperature (Tables 1 and 2). It is notable that a large amount of station records from the testing data have been assimilated by the ERA5 surface analysis scheme, which is coupled to the atmospheric model (Hersbach et al. 2020), and this should favor ERA5 when evaluating the relative performance of the MODIS-derived air temperature and ERA5. Despite this, with respective to the common independent in situ air measurements (the testing data in the neural network fitting model), ERA5 shows a smaller correlation and a higher bias than the reconstructed air temperature dataset, with an averaged R^2 of 0.96, averaged MB value of −0.30°C, and average MAE of 2.25°C. In terms of monthly R^2, eight out of twelve R^2 values from MODIS-derived air temperature are comparable to or slightly better than ERA5, which is similar to MAE, with the same or smaller values at eight months. Different from the MODIS-derived monthly air temperature (warm biases in nine months), ERA5 presents cold biases for spring, summer, and autumn, and warm biases for winter.

c. Spatiotemporal variability of near-surface air temperature over the AIS

Based on our reconstruction, spatial and temporal changes and trends in the AIS air temperature during 2001–18 are investigated. They are compared with those from ERA5, to further confirm the reliability of our reconstruction. Differences associated with the strengths and weaknesses of each method can be also further explored.

1) TEMPORAL VARIATION

We calculated the annual and seasonal mean air temperature anomalies of reconstruction, averaged over the Antarctic Peninsula (AP), the EAIS (East Antarctic ice sheet), and the WAIS (West Antarctic ice sheet), relative to their 2001–18 mean, respectively, to examine their interannual variations (Fig. 3). A set of somewhat different time series is obtained from ERA5 (Fig. 4). The linear trends in the time series of annual and seasonal mean near-surface air temperature from both datasets for the respective subregions are shown in Table 3. The 90% confidence level is used to test the statistical significance of these trends.

Large year-to-year fluctuations appear in the time series of annual mean temperature in the three regions of the AIS from 2001 to 2018, with different variation trends (see Figs. 3 and 4 and Table 3). Although on a regional scale, the magnitude of the reconstructed annual near-surface temperature trend is slightly different from that of ERA5, but their trend directions are the same. Furthermore, all the trends are not significant at the 90% confidence level. Over the EAIS, almost the same warming trend (0.10°C decade^{-1}) as ERA5 (0.07°C decade^{-1}) is observed from the reconstruction. However, the AP and WAIS show cooling trends (−0.23° and −0.09°C decade^{-1}, respectively). Compared with ERA5, the reconstructed temperature trend is 0.19°C decade^{-1} lower in the AP, but 0.04°C decade^{-1} higher for the WAIS. The reconstruction is more consistent with air temperature records based on a synthesis of six weather stations over the northern AP, revealing significant cooling from 1999 to 2014 (Turner et al. 2016). This is in contrast to the previously reported warming AP and WAIS from the late 1950s to the end of twentieth century or the early twenty-first century (e.g., Turner et al. 2005; Steig et al. 2009; Nicolas and Bromwich 2014).

In terms of seasonal averaged air temperature, their trends vary in sign and magnitude among different regions. In spring (SON), the reconstruction results are consistent with ERA5 results; both show warming on the EAIS, whereas obvious cooling occurs in the AP and WAIS ($p < 0.10$). However, our reconstruction results do indicate stronger cooling than
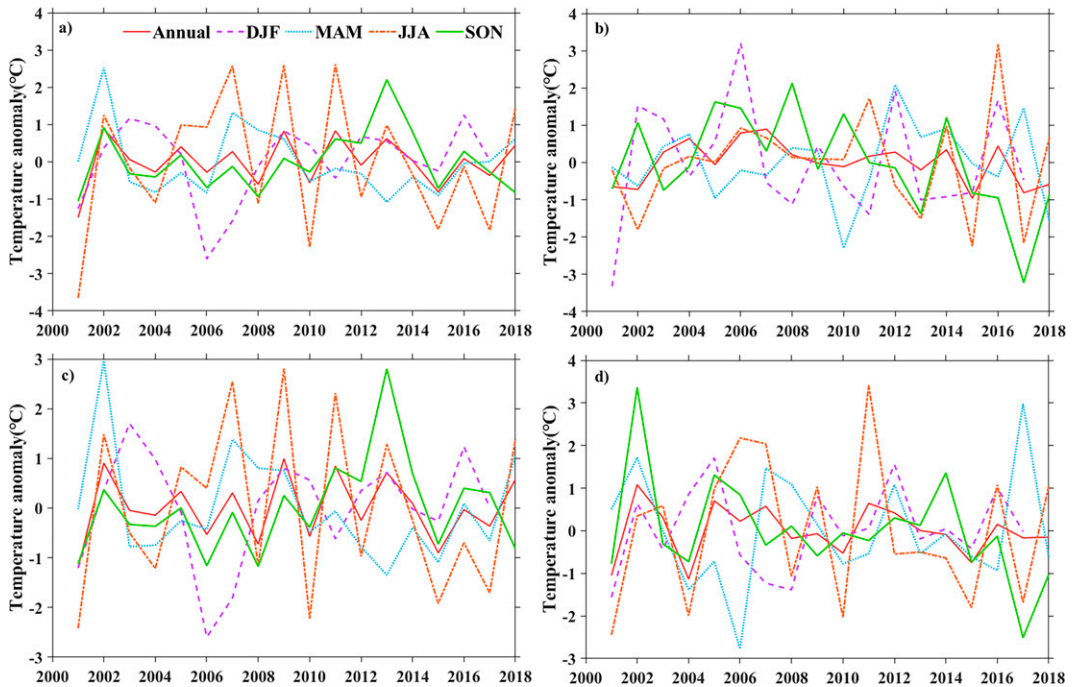
FIG. 3. Time series of annual and seasonal mean near-surface air temperature anomalies of reconstruction, spatially averaged over the (a) AIS, (b) AP, (c) EAIS, and (d) WAIS during 2001–18.

ERA5. In autumn (MAM) and winter (JJA), both datasets exhibit warming in the AP, with larger warming magnitude of ERA5 than reconstruction. In the same two seasons, cooling trends are both observed over the EAIS. But the cooling over

the WAIS depicted by ERA5 is in contrast to the warming seen in our reconstruction. The most significant differences between the reconstruction and ERA5 are found mainly in summer (DJF), with opposite temperature change trends in
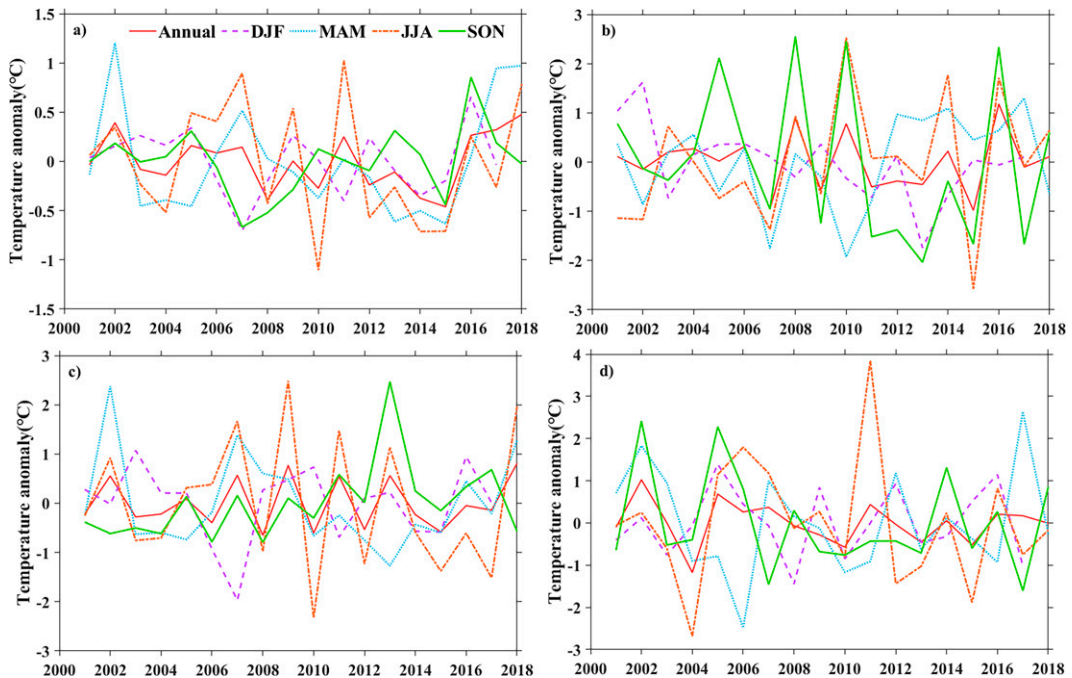

FIG. 4. Time series of annual and seasonal mean near-surface air temperature anomalies of ERA5, spatially averaged over the (a) AIS, (b) AP, (c) EAIS, and (d) WAIS during 2001–18.

TABLE 3. Linear treads (°C decade^{-1}) of near-surface air temperature from reconstruction and ERA5 over the three Antarctic subregions during 2001–18. Boldface font shows that the trend is significantly different from zero at the 90% confidence level.

Region	Annual	DJF	MAM	JJA	SON
Recon					
AP	−0.23 ± 0.05	−0.05 ± 0.16	0.18 ± 0.10	0.17 ± 0.13	**−1.12 ± 0.11**
EAIS	0.10 ± 0.06	0.34 ± 0.11	−0.52 ± 0.10	−0.09 ± 0.16	0.54 ± 0.08
WAIS	−0.09 ± 0.06	0.33 ± 0.10	0.10 ± 0.12	0.02 ± 0.16	**−0.95 ± 0.10**
ERA5					
AP	−0.04 ± 0.06	**−0.72 ± 0.06**	0.49 ± 0.08	0.64 ± 0.11	−0.63 ± 0.14
EAIS	0.07 ± 0.05	−0.08 ± 0.08	−0.19 ± 0.09	−0.20 ± 0.13	**0.61 ± 0.03**
WAIS	−0.13 ± 0.05	0.08 ± 0.08	−0.05 ± 0.11	−0.21 ± 0.14	−0.45 ± 0.10

the EAIS. And ERA5 shows even more significant cooling ($p < 0.10$) in the AP. The differences between reconstruction and ERA5 are somewhat expected given the cold bias that initially appeared in ERA5 temperature simulations.

2) SPATIAL VARIATION

Figures 5 and 6 show spatial distributions of the linear trends of annual and seasonal temperature during 2001–18 from our reconstruction and ERA5, respectively. The trend values of annual averaged temperature range from somewhat different to very different from one region to another, mainly due to the fact that the performance of ERA5 for air temperature is dependent on the availability of assimilated observations over the AIS. In the EAIS, the MODIS-derived annual temperature dataset presents significant warming trends (>0.4°C decade^{-1}, $p < 0.05$) in the 30°W–5°E sector of the Dronning Maud Land and along the coast of Victoria Land.

In contrast, significant cooling trends ($p < 0.05$) are observed in the 70°–150°E sector. These are almost the same as ERA5. But in the 40°–70°E sector, ERA5 shows a statistically significant warming trend, while the reconstructed trend is not obvious. The greatest difference occurs along east side of transantarctic mountains and Victoria Land, where ERA5 shows a statistically significant warming trend, not in our reconstruction. An overwhelming number of grid cells of the WAIS experience cooling trends, especially in the reconstruction with significant cooling trends in Mary Byrd Land (>0.4°C decade^{-1}, $p < 0.05$). However, a notable exception to general cooling over the WAIS is the inland area near transantarctic mountains, where exhibits strong and spatially coherent warming in both datasets.

The trends of near-surface air temperature at any season between 2001 and 2018 are spatially heterogeneous (Figs. 5 and 6b–e). In spring (SON), both reconstruction and ERA5 show that the EAIS has the maximal patches of significant
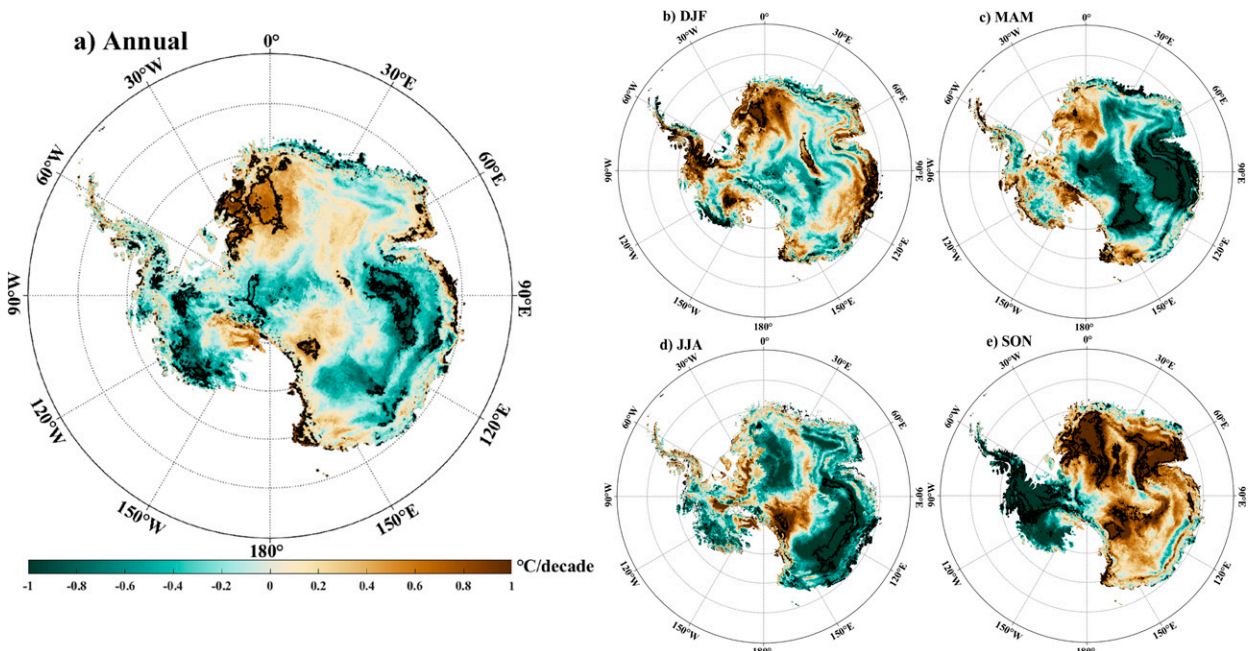

FIG. 5. Spatial distribution of trends in the (a) annual and (b)–(e) seasonal (summer, autumn, winter, and spring, respectively) mean near-surface air temperature of reconstruction for the 2001–18 period. The black lines outline the areas with trends significant at the 90% confidence interval.
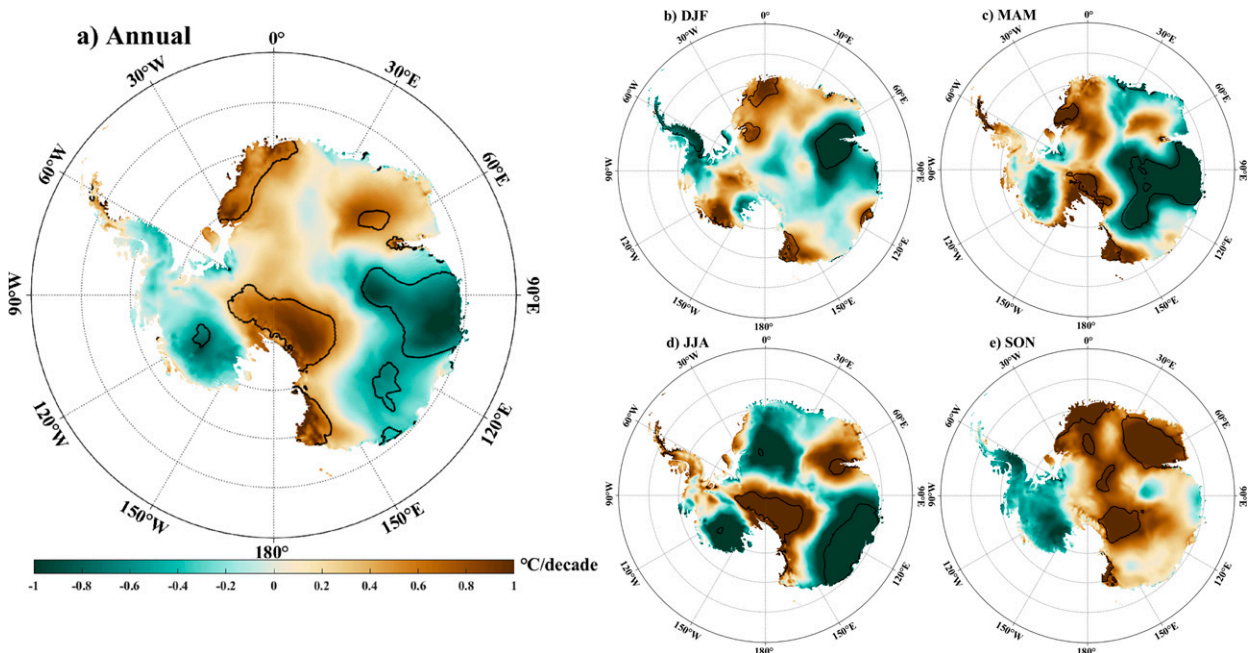
FIG. 6. Spatial distribution of trends in the (a) annual and (b)–(e) seasonal (summer, autumn, winter, and spring, respectively) mean near-surface air temperature of ERA5 for the 2001–18 period. The black lines outline the areas with trends significant at the 90% confidence interval.

warming, especially in the Dronning Maud Land and the 60°–70°E sector (>0.6°C decade^{-1}, $p < 0.05$). However, the AP and WAIS are dominated by the cooling trends, and are statistically significant in our reconstruction, not in ERA5. In summer (DJF), reconstruction and ERA5 indicate the cooling trends largely in the AP, the inland region of the 110°–150°E sector and part of WAIS coastal area, but warming trends in part of the WAIS, Dronning Maud Land, Victoria Land. However, across the 80°–100°E sector, contrary to the cooling trends shown by ERA5, the reconstructed significant warming trends are consistent with the coastal borehole temperature records (Roberts et al. 2013). Spatial distribution of MAM trends in the reconstruction and ERA5 are very similar to the annual trends, but with significantly stronger cooling trends in the part of 70°–150°E sector. During winter (JJA), the two show broadly consistent trend directions most of the AIS, but opposite temperature trends on the Lambert Glacier Basin. While AP warming is observed at both datasets, ERA5 reveals stronger and larger extent warming trends.

d. Influence of SAM on air temperature changes

The Southern Hemisphere annual mode (SAM) is the dominant mode of the Southern Hemisphere extratropical atmospheric circulation variability, which reflects a "seesaw" phenomenon of atmospheric variability, in which pressure and geopotential height vary in opposite phases between midlatitudes and high latitudes in the Southern Hemisphere (Thompson and Wallace 2000). SAM plays an important role in the climate system of the Antarctic region. Since the 1970s, the continuous strengthening of SAM to positive phase shifts in summer and autumn is considered as one of the main causes of air temperature changes in the EAIS (Thompson and Solomon 2002; Turner et al. 2005;

Marshall 2003; Thompson et al. 2011; Jones et al. 2019). In this study, we use the observed annual and seasonal SAM indices defined by Marshall (2003) to calculate the correlation coefficients between SAM and the near-surface temperature at each grid cell of our reconstruction (Fig. 7) and ERA5 (Fig. 8), which are used to investigate the possible influence of SAM on the near-surface temperature changes in Antarctica from 2001 to 2018.

Significant negative correlations between annual SAM and annual averaged air temperature appear in most of EAIS and WAIS, which suggests that year-to-year oscillation of annual temperature follows the opposite interannual patterns of SAM (Figs. 7 and 8). By comparison, the reconstruction has significantly higher correlations with SAM than ERA5. Similar patterns are observed in the WAIS and EAIS, except along the transantarctic mountains, and only slight differences can be observed in the AP, where opposite correlations happen in some grid cells. In autumn (MAM), both reconstruction and ERA5 show significant negative correlations between SAM and near-surface air temperatures in the EAIS, except for the western Dronning Maud Land and Victoria Land, whereas significant positive correlations occur in the northern AP, which is consistent with previous research (Marshall et al. 2006). This is mainly caused by the decrease of meridional heat exchange in the troposphere and downward turbulent heat flux near the surface of the ice sheet because of the enhancement of SAM positive phase, which leads to the cooling effect near the surface of most parts of the EAIS (van den Broeke and van Lipzig 2004). The SAM positive phase strengthens the Antarctic circumpolar wind and increases the transport of warm air to the AP, bringing a corresponding warming of the AP (Marshall et al. 2006; van Lipzig et al. 2008). There are no completely significant correlations between SAM and temperature in all
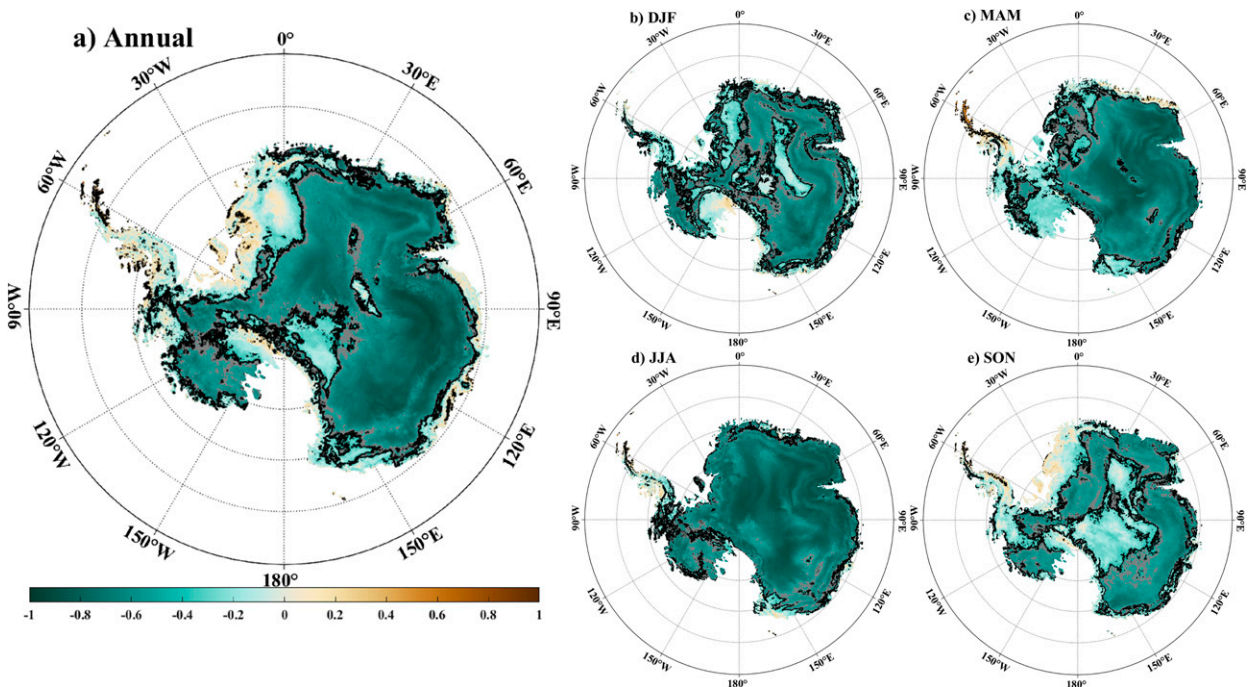
FIG. 7. Spatial distribution of correlation coefficients in the (a) annual and (b)–(e) seasonal (summer, autumn, winter, and spring, respectively) mean SAM indices and the corresponding near-surface temperature of reconstruction in the AIS. The black and gray lines outline the areas with trends significant at the confidence levels of 90% and 95%, respectively.

seasons except winter (JJA) in the 0°–60°W range of the EAIS, especially ERA5. The correlations between SAM and air temperature in any season are negative in most regions of the WAIS. In particular, the reconstruction is more significant, and the range of significant correlations is largest in winter. This implies that SAM-induced cooling effects also occur in the WAIS but may be altered by the Southern Oscillation/El Niño. In the AP, ERA5 shows a positive correlation between SAM and air temperature, especially in spring. On the contrary, in most regions of the AP excluding the northern AP, reconstruction shows that SAM is negatively and insignificantly correlated with temperature of almost all seasons. This seems to suggest little influence of the SAM on AP air temperature over these regions, which may be explained by the fact that the Weddell Sea is influenced by cyclones from midlatitude jet stream, resulting in high frequency of cold southeastern winds to blow toward the eastern AP and sea ice to move toward the eastern coast of the AP (Turner et al. 2016), which impedes warm northwesterly air caused by SAM onto the interior of the AP.

The results demonstrated above are consistent with and build on previous studies (Marshall 2007; Marshall and Thompson 2016; Fogt and Marshall 2020). Analysis confirms that SAM plays a key role in the regulation of Antarctic temperature on the year-to-year scale. And it has significant regional and seasonal differences in its effect on the near-surface temperature changes of the AIS. The strengthening positive phase of SAM has cooling effects to different extents on the EAIS and WAIS (except for the coastal areas of Berkner Island and Coats Land). On the contrary, SAM positive polarity results in the warming effect on the AP. The general pattern of a positive

(negative) correlation between SAM and near-surface temperature in Antarctica has been stable over the past half-century, but there are detailed differences between seasons. Marshall (2007) shows that during 1957–2004, SAM–temperature correlations are the most significant in autumn, and the spatial distribution pattern of correlations during winter are similar to those during autumn, but the magnitude of correlations decreases, which is contrary to our results (Marshall 2007).

4. Discussion

Because of the sparseness of in situ measurements in Antarctica, it is a challenging task to directly gather the observations to accurately reconstruct Antarctic near-surface air temperature fields. Here, we utilize the spatial covariance of surface temperature measurements from MODIS thermal infrared observations in combination with up-to-date AWS measurements for our near-surface air temperature reconstruction. The statistics of verification against independent measurements and the comparison with ERA5 reveal the robust quality of our reconstruction, because ERA5 represents the mean air temperature climatology best among the current global reanalysis products (Gossart et al. 2019).

Uncertainty estimation based on independent observations indicates less accurate air temperature reconstruction in winter than other seasons. This may be attributable to highly variable temperature conditions from the katabatic winds during winter (Nylen et al. 2004). Previous studies also reported the influence of wind speed on the relationship between the near-surface air temperature and surface skin temperature over the
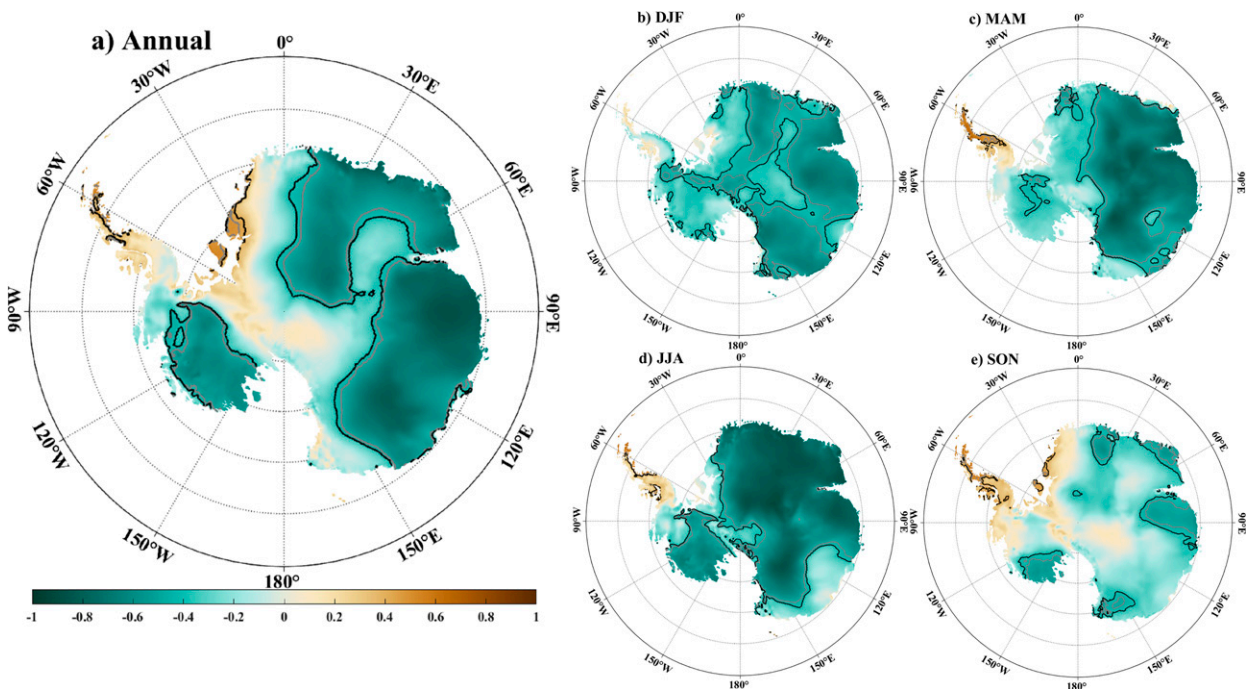
FIG. 8. Spatial distribution of correlation coefficients in the (a) annual and (b)–(e) seasonal (summer, autumn, winter, and spring, respectively) mean SAM indices and the corresponding near-surface temperature of ERA5 in the AIS. The black and gray lines outline the areas with trends significant at the confidence levels of 90% and 95%, respectively.

ice (e.g., Adolph et al. 2018; Nielsen-Englyst et al. 2019). Thus, the performance of the reconstruction should be improved if wind speed is used as one of the predictors. To do this, a high-quality Antarctic wind speed field is a prerequisite. However, current reanalyses and climate models usually suffer from representing katabatic winds with high accuracy and resolution in Antarctica (e.g., Rodrigo et al. 2013; Nygård et al. 2016; Dong et al. 2020), which possibly has an important impact on the accuracy of reconstruction. As Nielsen-Englyst et al. (2021) pointed out, even if the wind speed fields from ERA-Interim or ERA5 were included, the performance of Arctic air temperature reconstruction based on satellite-derived LST did not improve much.

Previous studies have reported that the accuracy of LST retrieval from satellite infrared data largely depends on the success of cloud masking (Comiso 2000). We further estimate the daily cloud contaminated MOD11C1 LST products using the measurements from seven weather stations located in the AP, Dronning Maud Land, and Berkner Island, respectively (Table 4). Robust correlations between MODIS retrievals and in situ LST measurements are found, with the correlation coefficients (R) of higher than 0.80 ($p < 0.05$). However, there are obvious deviations between the two types of LST measurements at each station site, with the MAE of 2.84°–3.91°C, and the larger MAE values occur on the coastal stations. All MB values are less than 0, meaning the underestimation by MODIS LST. The large deviation is mainly due to cloud contamination, which is not conducive to the reconstruction of near-surface temperature in Antarctica. Therefore, in order to reduce cloud interference, we make per-pixel quality control for MODIS LST products,

and extract LST pixels with good quality or fairly calibrated, so as to better correct atmospheric influence, and to further improve the accuracy of MODIS LST data.

We analyze near-surface air temperature trends at 62 stations with long continuous records (Fig. A1). The results are consistent with the trends inferred from our reconstruction. In annual trends, it is confirmed that there are strong and significant cooling trends in most stations of the AP and WAIS, but warming trends in the EAIS since 2000. In the seasonal temperature trends, the cooling is obvious in the AP, the WAIS, and the coast of the EAIS. In DJF and SON, most stations of the AP show significant cooling trends. In SON, Byrd Station, which has large fractions of temperature changes over the WAIS, also shows a cooling trend. In MAM and JJA, most stations of the EAIS also show statistically significant cooling trends. These findings are consistent with previous reported by Jones et al. (2019).

TABLE 4. Overall performance of the cloud contaminated MODIS LST by comparing with independent data. Statistically significant correlations above the 95% confidence level are denoted by two asterisks.

Station	Lat (°)	Lon (°)	R	MAE (°C)	MB (°C)
Latady	−70.9	−74.9	0.97**	3.76	−3.58
Wormold	−67.5	−68.1	0.93**	2.91	−2.56
Syowa	−69.0	39.6	0.83**	3.91	−2.71
AWS5	−73.1	−13.2	0.88**	3.66	−3.64
AWS6	−74.5	−11.5	0.89**	3.24	−3.21
AWS9	−75.0	0	0.93**	2.84	−2.57
AWS10	−79.6	−45.8	0.90**	3.80	−3.70

MODIS thermal infrared observations only provide clear-sky skin temperature measurements, not the temperatures under cloudy conditions, which often are present in the WAIS and over the ice sheet margins in October (Bromwich et al. 2012), and may provide no data at all on the floating ice shelves. This results in the gaps of reconstruction where MODIS data are unavailable due to the coverage of clouds, and even could cause spurious trends in the temperature reconstruction. However, the average coverage of clear-sky MODIS LST data exceeds 85% for the entire ice sheet during 2001–18, which means there are limited gaps of our reconstruction caused by clouds. This also suggest that a large fraction of information on all monthly near-surface air temperature is included in our reconstruction, despite the reconstruction derived from only clear-sky satellite observations. Statistical models can be used to fill in the gaps caused by clouds, as done by the European Union's Horizon 2020 project (EUSTACE) (Brugnara et al. 2019). However, gap filling is beyond the scope of this study.

5. Conclusions

In this study, we combine MODIS LST data with a neural network model to reconstruct a temporally and spatially continuous near-surface air temperature dataset of the AIS. The analysis shows that MODIS LST data are suitable for the estimation of near-surface air temperature. Validation against independent in situ observations reveals that the overall accuracy of the MODIS-based reconstruction is robust, with monthly MAE values of less than 2.45°C, R^2 of higher than 0.90, and MB values ranging from −0.19° to 0.32°C. In particular, the reconstructed temperature dataset presents higher accuracy than ERA5, a reanalysis dataset with smallest bias with respective to the observations than other global atmospheric reanalyses. Thus, we argue that the quality of our reconstruction is robust. Besides making up for the shortage of in situ observations, the MODIS-based air temperature reconstruction can be used as an important tool for data assimilation and validation of climate models, and has important applications for investigating the spatial and temporal patterns in air temperature changes in Antarctica and its possible connection with large-scale atmospheric circulation. In the future, it should be possible to further improve the model prediction accuracy by adding the other parameters such as wind speed and solar radiation into the reconstruction model. Nevertheless, before doing this, detailed investigation of the factors affecting the difference between air temperature and skin LST over Antarctica is required.

Our temperature reconstruction by means of satellite remote sensing data has greatly improved the spatial resolution of the reconstructed data. Based on the MODIS-based near-surface air temperature product, we find that annual cooling in the early twenty-first century extends from the AP to most of West Antarctica, and this is a much larger area than ever reported. This appears to show that global warming hiatus events also occur in these two regions. The examination of the impact of SAM on gridded temperature further confirms the spatial pattern of the SAM–temperature relationship reported in previous studies (Marshall 2007; Marshall and Thompson 2016; Fogt and Marshall 2020). The positive polarity of SAM has a warming effect on the AP, but a cooling effect on the EAIS and WAIS. Many sources may affect the SAM-related cooling, including anthropogenic factors such as stratospheric ozone depletion and increased greenhouse gas concentrations, as well as the role of natural variability in SAM changes, or the effect of ENSO on SAM, which contributes to climate change in Antarctica. Due to the complexity of the climate system, it is necessary to further explore the mechanism of the spatiotemporal variability of surface temperature in the AIS.

APPENDIX A

Main Characteristics of Weather Station and Station Observation Trends

Table A1 summarizes the coordinate, elevation, region, time span, station type, and data availability of 119 Antarctic weather stations, and their corresponding spatial distribution is shown in Fig. 1. Figure A1 presents the trends of annual and seasonal mean near-surface air temperature at 62 stations with records for the 2001–18 period.

APPENDIX B

Neural Network Fitting Model

In this paper, a two-layer feed-forward network with sigmoid hidden neurons and linear output neurons is used,

TABLE A1. Main characteristics of 119 weather stations. The number of each station is presented in Fig. 1.

No.	Station	Lat (°)	Lon (°)	Elevation (m)	Region	Period	Manned/AWS	Data availability (%)
1	AGO-4	−82.0	96.8	3597	EAIS	2012–18	AWS	97.6
2	Austin	−76.0	−87.5	1292	WAIS	2016–17	AWS	58.3
3	Baldrick	−82.8	−13.1	1968	EAIS	2008–18	AWS	91.7
4	Bear Peninsula	−74.5	−111.9	416	WAIS	2011–18	AWS	99.0
5	Brianna	−83.9	−134.2	520	WAIS	2000–15	AWS	62.5
6	Butler Island	−72.2	−60.2	91	AP	2000–12	AWS	91.0
7	Byrd	−80.0	−119.4	1539	WAIS	2000–18	AWS	79.4
8	Cape Bird	−77.2	166.4	38	EAIS	2000–18	AWS	78.5
9	Cape Denison	−67.0	142.7	31	EAIS	2000–11	AWS	25.0
10	Cape Hallett	−72.2	170.2	1	EAIS	2011–18	AWS	78.1
11	Clean Air	−90.0	0	2835	EAIS	2000–04	AWS	81.7
12	D_10	−66.7	139.8	243	EAIS	2000–18	AWS	53.5
13	D_47	−67.4	138.7	1560	EAIS	2008–18	AWS	88.6
14	D_85	−70.4	134.2	2651	EAIS	2009–18	AWS	65.0
15	Dome C II	−75.1	123.4	3250	EAIS	2000–18	AWS	95.2
16	Dome Fuji	−77.3	39.7	3810	EAIS	2002–18	AWS	71.1
17	Doug	−82.3	−113.2	1433	WAIS	2000–01	AWS	83.3
18	E-66	−68.9	134.6	2485	EAIS	2008–11	AWS	54.2
19	Elizabeth	−82.6	−137.1	523	WAIS	2000–18	AWS	56.1
20	Erin	−84.9	−128.9	988	WAIS	2000–18	AWS	73.7
21	Evans Knoll	−74.9	−100.4	178	WAIS	2011–18	AWS	95.8
22	Fossil Bluff	−71.3	−68.3	63	AP	2009–12	AWS	95.8
23	Harry	−83.0	−121.4	956	WAIS	2000–18	AWS	91.2
24	Henry	−89.0	−0.4	2781	EAIS	2000–17	AWS	83.8
25	Herbie Alley	−78.1	166.7	30	EAIS	2000–03	AWS	100
26	Janet	−77.2	−123.4	2085	WAIS	2011–18	AWS	91.7
27	JASE2007	−75.9	25.8	3661	EAIS	2000–18	AWS	92.4
28	Kathie	−78.0	−97.3	1607	WAIS	2016–18	AWS	97.2
29	Kominko-Slade	−79.5	−112.1	1801	WAIS	2007–18	AWS	83.3
30	Marble Point II	−77.4	163.8	111	EAIS	2011–18	AWS	81.3
31	Marble Point	−77.4	163.8	108	EAIS	2000–18	AWS	100
32	Marlene	−83.6	−167.4	83	WAIS	2011–14	AWS	91.7
33	Minna Bluff	−78.6	166.7	895	EAIS	2000–18	AWS	82.0
34	Mizuho	−70.7	44.3	2260	EAIS	2000–18	AWS	94.3
35	Mount Fleming	−77.5	160.3	1868	EAIS	2008–10	AWS	75.0
36	Mulock	−79.0	160.2	378	EAIS	2006–11	AWS	45.8
37	Nico	−89.0	90.0	2979	EAIS	2000–17	AWS	82.9
38	Noel	−79.3	−111.1	1833	WAIS	2000–2000	AWS	41.7
39	PANDA-South	−82.3	76.0	4027	EAIS	2008–18	AWS	23.5
40	Penguin Point	−67.6	146.2	30	EAIS	2000–02	AWS	77.8
41	Port Martin	−66.8	141.4	39	EAIS	2000–17	AWS	25.0
42	Possession Island	−71.9	171.2	30	EAIS	2000–18	AWS	89.9
43	Relay Station	−74.0	43.1	3353	EAIS	2000–18	AWS	77.2
44	Siple Dome	−81.7	−149.0	667	WAIS	2000–18	AWS	79.8
45	Sky Blu	−74.8	−71.5	1510	AP	2000–12	AWS	52.6
46	Sutton	−67.1	141.4	871	EAIS	2000–2000	AWS	58.3
47	Swithinbank	−81.2	−126.2	959	WAIS	2000–10	AWS	36.4
48	Theresa	−84.6	−115.9	1454	WAIS	2000–18	AWS	85.5
49	Tom	−84.4	−171.5	79	EAIS	2011–14	AWS	62.5
50	Uranus Glacier	−71.4	−68.8	753	AP	2000–03	AWS	70.8
51	White Island	−78.1	167.5	686	EAIS	2015–18	AWS	79.2
52	Windless Bight	−77.7	167.7	40	EAIS	2000–18	AWS	72.4
53	A028-B	−68.4	112.2	1622	EAIS	2000–05	AWS	93.1
54	Apfel	−66.3	100.8	150	EAIS	2000–01	AWS	75.0
55	Aurora Basin North	−71.2	111.4	2714	EAIS	2014–17	AWS	70.8
56	Brown Glacier, Heard Island	−53.1	73.6	640	EAIS	2000–02	AWS	61.1
57	Dome_A	−80.4	77.4	4084	EAIS	2005–17	AWS	95.5
58	DSS	−66.8	112.8	1376	EAIS	2000–05	AWS	86.1
59	Eagle	−76.4	77.0	2830	EAIS	2005–17	AWS	96.2

TABLE A1. (*Continued*)

| No.	Station	Lat (°)	Lon (°)	Elevation (m)	Region	Period	Manned/AWS	Data availability (%)
60	Eder_Island	−67.0	143.9	52	EAIS	2000–2000	AWS	75.0
61	GC41	−71.6	111.3	2791	EAIS	2000–05	AWS	98.6
62	GF08-A	−68.5	102.2	2123	EAIS	2000–07	AWS	95.8
63	Lanyon-A	−66.3	110.8	390	EAIS	2000–08	AWS	87.0
64	LGB00-C	−68.7	61.1	1830	EAIS	2000–09	AWS	92.5
65	LGB10-A	−71.3	59.2	2620	EAIS	2000–06	AWS	86.9
66	LGB20	−73.8	55.7	2741	EAIS	2000–04	AWS	93.3
67	LGB35	−76.0	65.0	2342	EAIS	2000–08	AWS	94.4
68	LGB59	−73.5	76.8	2537	EAIS	2000–04	AWS	88.3
69	LGB69	−70.8	77.1	1854	EAIS	2002–08	AWS	84.5
70	MtBrown	−69.1	86.0	2064	EAIS	2000–11	AWS	74.3
71	Panda	−74.7	77.0	2584	EAIS	2008–17	AWS	51.7
72	Ranvik	−68.9	78.0	339	EAIS	2000–01	AWS	87.5
73	Rumdoodle	−67.7	62.8	430	EAIS	2000–01	AWS	95.8
74	Amundsen_Scott	−90.0	0	2835	EAIS	2000–18	Manned	100
75	Arturo_Prat	−62.5	−59.7	5	AP	2000–18	Manned	62.3
76	Belgrano_II	−77.9	−34.6	256	EAIS	2000–18	Manned	71.1
77	Bellingshausen	−62.2	−58.9	16	AP	2000–18	Manned	100
78	Casey	−66.3	110.5	42	EAIS	2000–18	Manned	99.6
79	Dumont_Durville	−66.7	140.0	43	EAIS	2000–18	Manned	87.3
80	Esperanza	−63.4	−57.0	13	AP	2000–18	Manned	99.6
81	Ferraz	−62.1	−58.4	20	AP	2000–05	Manned	95.8
82	Great_Wall	−62.2	−59.0	10	AP	2000–18	Manned	95.2
83	Jubany	−62.2	−58.6	4	AP	2000–18	Manned	87.7
84	King_Sejong	−62.2	−58.7	11	AP	2000–17	Manned	58.8
85	Marambio	−64.2	−56.7	198	AP	2000–18	Manned	99.1
86	Mario_Zucchelli	−74.7	164.1	92	EAIS	2000–18	Manned	68.0
87	Marsh	−62.2	−58.9	10	AP	2000–18	Manned	89.5
88	Mawson	−67.6	62.9	16	EAIS	2000–18	Manned	99.6
89	Molodeznaja	−67.7	45.9	40	EAIS	2014–18	Manned	36.7
90	Novolazarevskaya	−70.8	11.8	119	EAIS	2000–18	Manned	99.6
91	O_Higgins	−63.3	−57.9	10	AP	2000–18	Manned	73.7
92	Orcadas	−60.7	−44.7	6	AP	2000–18	Manned	88.6
93	Rothera	−67.5	−68.1	32	AP	2000–18	Manned	99.6
94	San_Martin	−68.1	−67.1	4	AP	2000–18	Manned	84.2
95	Syowa	−69.0	39.6	21	EAIS	2000–18	Manned	100
96	Vostok	−78.5	106.9	3490	EAIS	2000–18	Manned	92.1
97	Zhongshan	−69.4	76.4	18	EAIS	2000–18	Manned	99.1
98	Arelis	−76.7	163.0	150	EAIS	2000–18	AWS	100
99	Concordia	−74.5	123.0	3280	EAIS	2005–18	AWS	91.1
100	Eneide	−74.7	164.1	92	EAIS	2000–18	AWS	99.6
101	Giulia	−75.6	145.8	2200	EAIS	2000–18	AWS	62.3
102	Irene	−71.6	148.7	2000	EAIS	2001–15	AWS	50.6
103	Jennica	−74.7	164.1	92	EAIS	2000–03	AWS	39.6
104	Lola	−74.1	163.4	1621	EAIS	2000–18	AWS	95.2
105	Maria	−74.6	164.0	355	EAIS	2000–18	AWS	65.4
106	Modesta	−73.6	160.7	1924	EAIS	2000–18	AWS	83.3
107	Paola	−72.8	159.0	0	EAIS	2003–18	AWS	47.4
108	Rita	−74.7	164.0	268	EAIS	2000–18	AWS	92.5
109	Silvia	−73.5	169.7	536	EAIS	2000–18	AWS	84.2
110	Zoraida	−74.2	162.9	644	EAIS	2000–18	AWS	72.8
111	AWS5	−73.1	−13.2	360	EAIS	2000–14	AWS	93.9
112	AWS6	−74.5	−11.5	1160	EAIS	2000–09	AWS	90.8
113	AWS8	−76.0	−8.1	2400	EAIS	2000–02	AWS	100
114	AWS9	−75.0	0	2900	EAIS	2000–18	AWS	94.3
115	AWS10	−79.6	−45.8	890	WAIS	2000–05	AWS	55.6
116	AWS11	−71.2	−6.8	690	EAIS	2007–15	AWS	76.9
117	AWS12	−78.7	35.6	3620	EAIS	2008–16	AWS	90.7
118	AWS13	−82.1	55.0	3730	EAIS	2008–15	AWS	100
119	AWS16	−72.0	23.3	1300	EAIS	2009–15	AWS	82.1
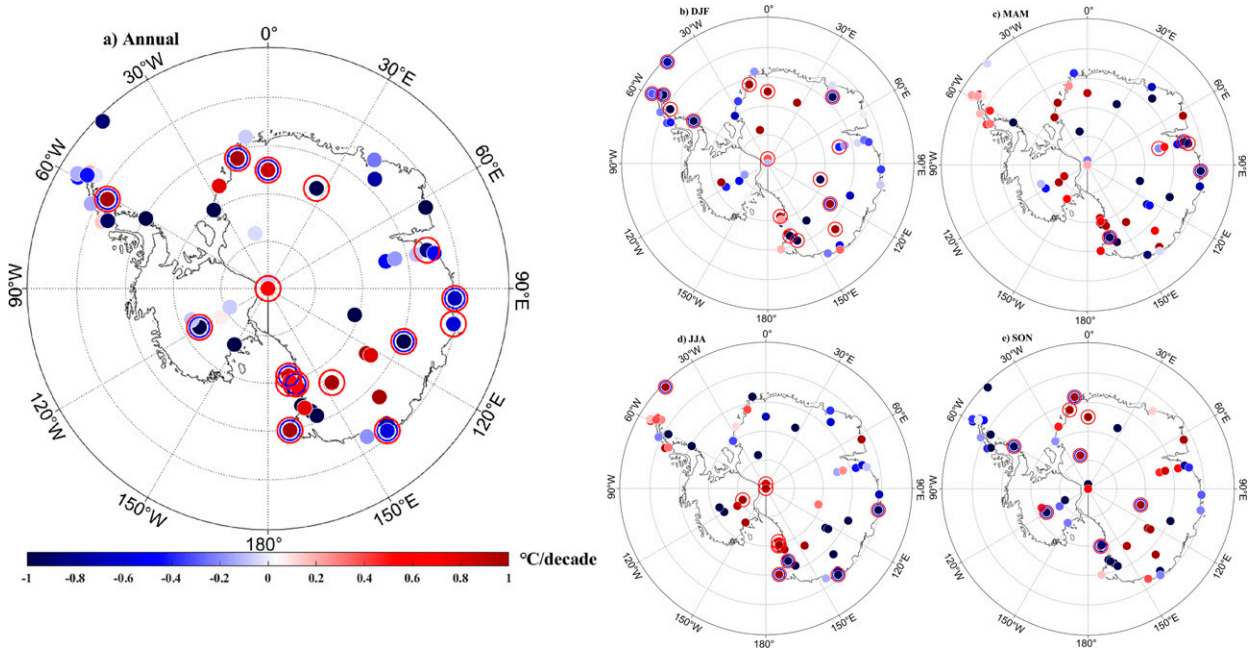
FIG. A1. Spatial distribution of trends in the (a) annual and (b)–(e) seasonal (summer, autumn, winter, and spring, respectively) station-based mean near-surface air temperature for the 2001–18 period. The red and blue circles outline the stations with trends significant at 90% and 95% confidence level, respectively.

which can fit mapping problems arbitrarily well, and give consistent data and enough neurons in its hidden layer (Jang et al. 2004; Chronopoulos et al. 2008). By constructing algorithms and functions of typical neural networks, we can build, train, visualize, and simulate networks for specific network structures.

A single hidden layer neural network is used to fit the model. Assuming that the number of neurons in the hidden layer is i ($i = 10$), the number of neurons in the output layer is 1, x_i is the i input of the neuron, the threshold value of neurons is Θ, w_i is the connection weight of the hidden layer and the output layer, then the output y of neurons is as follows:

$$ y = f\left(\sum_{i}^{10} w_i x_i - \theta\right), \tag{B1} $$

where f is the activation function of neurons, and the sigmoid function is adopted in this paper; that is, $f = 1/(1 + e^{-x})$. The network learning function is set as Learngdm, and the network training function is set as Trainlm. The corresponding Levenberg–Marquardt algorithm is used, which usually requires more memory but less time (Hagan and Menhaj 1994; Tan and Van Cauwenberghe 1999).

If the expected output mode is not obtained in the output layer by forward propagation, the process is turned to error back propagation. The gradient descent method (namely, the Traingd function) is used to adjust the weighted w_i. After repeated learning and training, the error signal is minimized. A premature termination strategy is used to prevent the occurrence of overfitting (McCord-Nelson and Illingworth 1991; Prechelt 1998). Training automatically stops when generalization

stops improving, as indicated by an increase in the mean square error of the validation samples. Due to differences in initial conditions and samples, multiple training sessions will produce different results.

REFERENCES

Adolph, A. C., M. R. Albert, and D. K. Hall, 2018: Near-surface temperature inversion during summer at Summit, Greenland, and its relation to MODIS-derived surface temperatures. *Cryosphere*, **12**, 907–920, https://doi.org/10.5194/tc-12-907-2018.

Araújo, R. D. A., A. L. Oliveira, and S. Meira, 2017: A morphological neural network for binary classification problems. *Eng. Appl. Artif. Intell.*, **65**, 12–28, https://doi.org/10.1016/j.engappai.2017.07.014.

Benali, A., A. C. Carvalho, J. P. Nunes, N. Carvalhais, and A. Santos, 2012: Estimating air surface temperature in Portugal using MODIS LST data. *Remote Sens. Environ.*, **124**, 108–121, https://doi.org/10.1016/j.rse.2012.04.024.

Bromwich, D. H., J. P. Nicolas, K. M. Hines, J. E. Kay, E. L. Key, M. A. Lazzara, and N. P. van Lipzig, 2012: Tropospheric clouds in Antarctica. *Rev. Geophys.*, **50**, RG1004, https://doi.org/10.1029/2011RG000363.

Brugnara, Y., E. Good, A. A. Squintu, G. van der Schrier, and S. Brönnimann, 2019: The EUSTACE global land station daily air temperature dataset. *Geosci. Data J.*, **6**, 189–204, https://doi.org/10.1002/gdj3.81.

Cannone, N., M. Guglielmin, P. Convey, M. R. Worland, and S. F. Longo, 2016: Vascular plant changes in extreme environments: Effects of multiple drivers. *Climatic Change*, **134**, 651–665, https://doi.org/10.1007/s10584-015-1551-7.

Chronopoulos, K. I., I. X. Tsiros, I. F. Dimopoulos, and N. Alvertos, 2008: An application of artificial neural network models to

estimate air temperature data in areas with sparse network of meteorological stations. *J. Environ. Sci. Health*, **43**, 1752–1757, https://doi.org/10.1080/10934520802507621.

Comiso, J. C., 2000: Variability and trends in Antarctic surface temperatures from in situ and satellite infrared measurements. *J. Climate*, **13**, 1674–1696, https://doi.org/10.1175/1520-0442(2000)013<1674:VATIAS>2.0.CO;2.

Convey, P., S. J. Coulson, M. R. Worland, and A. Sjöblom, 2018: The importance of understanding annual and shorter-term temperature patterns and variation in the surface levels of polar soils for terrestrial biota. *Polar Biol.*, **41**, 1587–1605, https://doi.org/10.1007/s00300-018-2299-0.

Costanza, C. A., M. A. Lazzara, L. M. Keller, and J. J. Cassano, 2016: The surface climatology of the Ross Ice Shelf Antarctica. *Int. J. Climatol.*, **36**, 4929–4941, https://doi.org/10.1002/joc.4681.

Coulibaly, P., F. Anctil, and B. Bobée, 2000: Daily reservoir inflow forecasting using artificial neural networks with stopped training approach. *J. Hydrol.*, **230**, 244–257, https://doi.org/10.1016/S0022-1694(00)00214-6.

Deb, P., A. Orr, J. S. Hosking, T. Phillips, J. Turner, D. Bannister, J. O. Pope, and S. Colwell, 2016: An assessment of the Polar Weather Research and Forecasting (WRF) model representation of near-surface meteorological variables over West Antarctica. *J. Geophys. Res. Atmos.*, **121**, 1532–1548, https://doi.org/10.1002/2015JD024037.

Dong, X., Y. Wang, S. Hou, M. Ding, B. Yin, and Y. Zhang, 2020: Robustness of the recent global atmospheric reanalyses for Antarctic near-surface wind speed climatology. *J. Climate*, **33**, 4027–4043, https://doi.org/10.1175/JCLI-D-19-0648.1.

Fogt, R. L., and G. J. Marshall, 2020: The southern annular mode: Variability, trends, and climate impacts across the Southern Hemisphere. *Wiley Interdiscip. Rev.: Climate Change*, **11**, e652, https://doi.org/10.1002/wcc.652.

Fréville, H., E. Brun, G. Picard, N. Tatarinova, L. Arnaud, C. Lanconelli, and M. van den Broeke, 2014: Using MODIS land surface temperatures and the Crocus snow model to understand the warm bias of ERA-Interim reanalyses at the surface in Antarctica. *Cryosphere*, **8**, 1361–1373, https://doi.org/10.5194/tc-8-1361-2014.

Gallée, H., and I. V. Gorodetskaya, 2010: Validation of a limited area model over Dome C, Antarctic Plateau, during winter. *Climate Dyn.*, **34**, 61–72, https://doi.org/10.1007/s00382-008-0499-y.

Genthon, C., and G. Krinner, 2001: Antarctic surface mass balance and systematic biases in general circulation models. *J. Geophys. Res.*, **106**, 20 653–20 664, https://doi.org/10.1029/2001JD900136.

Gossart, A., S. Helsen, J. T. M. Lenaerts, S. van den Broucke, N. P. M. van Lipzig, and N. Souverijns, 2019: An evaluation of surface climatology in state-of-the-art reanalyses over the Antarctic Ice Sheet. *J. Climate*, **32**, 6899–6915, https://doi.org/10.1175/JCLI-D-19-0030.1.

Guo, Z., D. H. Bromwich, and J. J. Cassano, 2003: Evaluation of Polar MM5 simulations of Antarctic atmospheric circulation. *Mon. Wea. Rev.*, **131**, 384–411, https://doi.org/10.1175/1520-0493(2003)131<0384:EOPMSO>2.0.CO;2.

Hagan, M. T., and M. B. Menhaj, 1994: Training feedforward networks with the Marquardt algorithm. *IEEE Trans. Neural Netw.*, **5**, 989–993, https://doi.org/10.1109/72.329697.

Herbei, R., A. L. Rytel, W. B. Lyons, D. M. McKnight, C. Jaros, M. N. Gooseff, and J. C. Priscu, 2016: Hydrological controls on ecosystem dynamics in Lake Fryxell, Antarctica. *PLOS ONE*, **11**, e0159038, https://doi.org/10.1371/journal.pone.0159038.

Hersbach, H., B. Bell, P. Berrisford, S. Hirahara, A. Horányi, J. Muñoz-Sabater, and J. N. Thépaut, 2020: The ERA5 global reanalysis. *Quart. J. Roy. Meteor. Soc.*, **146**, 1999–2049, https://doi.org/10.1002/qj.3803.

Hooker, J., G. Duveiller, and A. Cescatti, 2018: A global dataset of air temperature derived from satellite remote sensing and weather stations. *Sci. Data*, **5**, 180246, https://doi.org/10.1038/sdata.2018.246.

Huai, B., Y. Wang, M. Ding, J. Zhang, and X. Dong, 2019: An assessment of recent global atmospheric reanalyses for Antarctic near surface air temperature. *Atmos. Res.*, **226**, 181–191, https://doi.org/10.1016/j.atmosres.2019.04.029.

Jang, J. D., A. A. Viau, and F. Anctil, 2004: Neural network estimation of air temperatures from AVHRR data. *Int. J. Remote Sens.*, **25**, 4541–4554, https://doi.org/10.1080/01431160310001657533.

Jones, M. E., D. H. Bromwich, J. P. Nicolas, J. Carrasco, E. Plavcová, X. Zou, and S. H. Wang, 2019: Sixty years of widespread warming in the southern middle and high latitudes (1957–2016). *J. Climate*, **32**, 6875–6898, https://doi.org/10.1175/JCLI-D-18-0565.1.

Kilibarda, M., T. Hengl, G. B. Heuvelink, B. Gräler, E. Pebesma, M. Perčec Tadić, and B. Bajat, 2014: Spatio-temporal interpolation of daily temperatures for global land areas at 1 km resolution. *J. Geophys. Res. Atmos.*, **119**, 2294–2313, https://doi.org/10.1002/2013JD020803.

Kwok, R., and J. C. Comiso, 2002: Spatial patterns of variability in Antarctic surface temperature: Connections to the Southern Hemisphere annular mode and the southern oscillation. *Geophys. Res. Lett.*, **29**, 50-1–51-4, https://doi.org/10.1029/2002GL015415.

Lazzara, M. A., G. A. Weidner, L. M. Keller, J. E. Thom, and J. J. Cassano, 2012: Antarctic automatic weather station program: 30 years of polar observation. *Bull. Amer. Meteor. Soc.*, **93**, 1519–1537, https://doi.org/10.1175/BAMS-D-11-00015.1.

Liang, Y. C., C. Frankignoul, Y. O. Kwon, G. Gastineau, E. Manzini, G. Danabasoglu, and Y. Zhang, 2021: Impacts of Arctic sea ice on cold season atmospheric variability and trends estimated from observations and a multi-model large ensemble. *J. Climate*, **34**, 8419–8443, https://doi.org/10.1175/JCLI-D-20-0578.1.

Marshall, G. J., 2003: Trends in the southern annular mode from observations and reanalyses. *J. Climate*, **16**, 4134–4143, https://doi.org/10.1175/1520-0442(2003)016<4134:TITSAM>2.0.CO;2.

——, 2007: Half-century seasonal relationships between the southern annular mode and Antarctic temperatures. *Int. J. Climatol.*, **27**, 373–383, https://doi.org/10.1002/joc.1407.

——, and D. W. J. Thompson, 2016: The signatures of large-scale patterns of atmospheric variability in Antarctic surface temperatures. *J. Geophys. Res. Atmos.*, **121**, 3276–3289, https://doi.org/10.1002/2015JD024665.

——, A. Orr, N. P. van Lipzig, and J. C. King, 2006: The impact of a changing Southern Hemisphere annular mode on Antarctic Peninsula summer temperatures. *J. Climate*, **19**, 5388–5404, https://doi.org/10.1175/JCLI3844.1.

McCord-Nelson, M., and W. T. Illingworth, 1991: *A Practical Guide to Neural Nets*. Addison-Wesley Longman, 344 pp.

McCulloch, W. S., and W. Pitts, 1943: A logical calculus of the ideas immanent in nervous activity. *Bull. Math. Biophys.*, **5**, 115–133, https://doi.org/10.1007/BF02478259.

Monaghan, A. J., D. H. Bromwich, W. Chapman, and J. C. Comiso, 2008: Recent variability and trends of Antarctic near-surface

temperature. *J. Geophys. Res.*, **113**, D04105, https://doi.org/10.1029/2007JD009094.

Mostovoy, G. V., R. L. King, K. R. Reddy, V. G. Kakani, and M. G. Filippova, 2006: Statistical estimation of daily maximum and minimum air temperatures from MODIS LST data over the state of Mississippi. *GIsci. Remote Sens.*, **43**, 78–110, https://doi.org/10.2747/1548-1603.43.1.78.

Neteler, M., 2010: Estimating daily land surface temperatures in mountainous environments by reconstructed MODIS LST data. *Remote Sens.*, **2**, 333–351, https://doi.org/10.3390/rs1020333.

Nicolas, J. P., and D. H. Bromwich, 2014: New reconstruction of Antarctic near-surface temperatures: Multidecadal trends and reliability of global reanalyses. *J. Climate*, **27**, 8070–8093, https://doi.org/10.1175/JCLI-D-13-00733.1.

Nielsen-Englyst, P., J. L. Høyer, K. S. Madsen, R. Tonboe, G. Dybkjær, and E. Alerskans, 2019: In situ observed relationships between snow and ice surface skin temperatures and 2 m air temperatures in the Arctic. *Cryosphere*, **13**, 1005–1024, https://doi.org/10.5194/tc-13-1005-2019.

——, ——, ——, R. T. Tonboe, G. Dybkjær, and S. Skarpalezos, 2021: Deriving Arctic 2 m air temperatures over snow and ice from satellite surface temperature measurements. *Cryosphere*, **15**, 3035–3057, https://doi.org/10.5194/tc-15-3035-2021.

Noël, B., and Coauthors, 2018: Modelling the climate and surface mass balance of polar ice sheets using RACMO2—Part 1: Greenland (1958–2016). *Cryosphere*, **12**, 811–831, https://doi.org/10.5194/tc-12-811-2018.

Nygård, T., T. Vihma, G. Birnbaum, J. Hartmann, J. King, T. Lachlan-Cope, and A. Weiss, 2016: Validation of eight atmospheric reanalyses in the Antarctic Peninsula region. *Quart. J. Roy. Meteor. Soc.*, **142**, 684–692, https://doi.org/10.1002/qj.2691.

Nylen, T. H., A. G. Fountain, and P. T. Doran, 2004: Climatology of katabatic winds in the McMurdo dry valleys, southern Victoria Land, Antarctica. *J. Geophys. Res.*, **109**, D03114, https://doi.org/10.1029/2003JD003937.

Prechelt, L., 1998: Automatic early stopping using cross validation: Quantifying the criteria. *Neural Network*, **11**, 761–767, https://doi.org/10.1016/S0893-6080(98)00010-0.

Roberts, J. L., A. D. Moy, T. D. van Ommen, M. A. J. Curran, A. P. Worby, I. D. Goodwin, and M. Inoue, 2013: Borehole temperatures reveal a changed energy budget at Mill Island, East Antarctica, over recent decades. *Cryosphere*, **7**, 263–273, https://doi.org/10.5194/tc-7-263-2013.

Rodrigo, J. S., J. M. Buchlin, J. van Beeck, J. T. Lenaerts, and M. R. van den Broeke, 2013: Evaluation of the Antarctic surface wind climate from ERA reanalyses and RACMO2/ANT simulations based on automatic weather stations. *Climate Dyn.*, **40**, 353–376, https://doi.org/10.1007/s00382-012-1396-y.

Ruiz, L. G. B., M. P. Cuéllar, M. D. Calvo-Flores, and M. D. C. P. Jiménez, 2016: An application of non-linear autoregressive neural networks to predict energy consumption in public buildings. *Energies*, **9**, 684, https://doi.org/10.3390/en9090684.

Sánchez, D., P. Melin, and O. Castillo, 2017: Optimization of modular granular neural networks using a firefly algorithm for human recognition. *Eng. Appl. Artif. Intell.*, **64**, 172–186, https://doi.org/10.1016/j.engappai.2017.06.007.

Schneider, D. P., E. J. Steig, and J. C. Comiso, 2004: Recent climate variability in Antarctica from satellite-derived temperature data. *J. Climate*, **17**, 1569–1583, https://doi.org/10.1175/1520-0442(2004)017<1569:RCVIAF>2.0.CO;2.

Steig, E. J., D. P. Schneider, S. D. Rutherford, M. E. Mann, J. C. Comiso, and D. T. Shindell, 2009: Warming of the Antarctic ice-sheet surface since the 1957 International Geophysical Year. *Nature*, **457**, 459–462, https://doi.org/10.1038/nature07669.

Tan, Y., and A. Van Cauwenberghe, 1999: Neural-network-based *d*-step-ahead predictors for nonlinear systems with time delay. *Eng. Appl. Artif. Intell.*, **12**, 21–35, https://doi.org/10.1016/S0952-1976(98)00043-8.

Tastula, E. M., and T. Vihma, 2011: WRF model experiments on the Antarctic atmosphere in winter. *Mon. Wea. Rev.*, **139**, 1279–1291, https://doi.org/10.1175/2010MWR3478.1.

——, ——, and E. L Andreas, 2012: Evaluation of Polar WRF from modeling the atmospheric boundary layer over Antarctic sea ice in autumn and winter. *Mon. Wea. Rev.*, **140**, 3919–3935, https://doi.org/10.1175/MWR-D-12-00016.1.

Thompson, D. W., and J. M. Wallace, 2000: Annular modes in the extratropical circulation. Part I: Month-to-month variability. *J. Climate*, **13**, 1000–1016, https://doi.org/10.1175/1520-0442(2000)013<1000:AMITEC>2.0.CO;2.

——, and S. Solomon, 2002: Interpretation of recent Southern Hemisphere climate change. *Science*, **296**, 895–899, https://doi.org/10.1126/science.1069270.

——, ——, P. J. Kushner, M. H. England, K. M. Grise, and D. J. Karoly, 2011: Signatures of the Antarctic ozone hole in Southern Hemisphere surface climate change. *Nat. Geosci.*, **4**, 741–749, https://doi.org/10.1038/ngeo1296.

Trusel, L. D., K. E. Frey, S. B. Das, K. B. Karnauskas, P. K. Munneke, E. Van Meijgaard, and M. R. van den Broeke, 2015: Divergent trajectories of Antarctic surface melt under two twenty-first-century climate scenarios. *Nat. Geosci.*, **8**, 927–932, https://doi.org/10.1038/ngeo2563.

Turner, J., and Coauthors, 2004: The SCAR READER project: Toward a high-quality database of mean Antarctic meteorological observations. *J. Climate*, **17**, 2890–2898, https://doi.org/10.1175/1520-0442(2004)017<2890:TSRPTA>2.0.CO;2.

——, S. R. Colwell, G. J. Marshall, T. A. Lachlan-Cope, A. M. Carleton, P. D. Jones, and S. Iagovkina, 2005: Antarctic climate change during the last 50 years. *Int. J. Climatol.*, **25**, 279–294, https://doi.org/10.1002/joc.1130.

——, H. Lu, I. White, J. C. King, T. Phillips, J. S. Hosking, and P. Deb, 2016: Absence of 21st century warming on Antarctic Peninsula consistent with natural variability. *Nature*, **535**, 411–415, https://doi.org/10.1038/nature18645.

Vancutsem, C., P. Ceccato, T. Dinku, and S. J. Connor, 2010: Evaluation of MODIS land surface temperature data to estimate air temperature in different ecosystems over Africa. *Remote Sens. Environ.*, **114**, 449–465, https://doi.org/10.1016/j.rse.2009.10.002.

van den Broeke, M. R., and N. P. van Lipzig, 2004: Changes in Antarctic temperature, wind and precipitation in response to the Antarctic Oscillation. *Ann. Glaciol.*, **39**, 119–126, https://doi.org/10.3189/172756404781814654.

van Lipzig, N. P. M., J. C. King, T. A. Lachlan-Cope, and M. R. van den Broeke, 2004a: Precipitation, sublimation, and snow drift in the Antarctic Peninsula region from a regional atmospheric model. *J. Geophys. Res.*, **109**, D24106, https://doi.org/10.1029/2004JD004701.

——, J. Turner, S. R. Colwell, and M. R. van den Broeke, 2004b: The near-surface wind field over the Antarctic continent. *Int. J. Climatol.*, **24**, 1973–1982, https://doi.org/10.1002/joc.1090.

——, G. J. Marshall, A. Orr, and J. C. King, 2008: The relationship between the Southern Hemisphere annular mode and Antarctic Peninsula summer temperatures: Analysis of a

high-resolution model climatology. *J. Climate*, **21**, 1649–1668, https://doi.org/10.1175/2007JCLI1695.1.

Wan, Z., 2013: *Collection-6 MODIS Land Surface Temperature Products Users' Guide*. 33 pp., https://lpdaac.usgs.gov/documents/118/MOD11_User_Guide_V6.pdf.

——, 2014: New refinements and validation of the Collection-6 MODIS land-surface temperature/emissivity product. *Remote Sens. Environ.*, **140**, 36–45, https://doi.org/10.1016/j.rse.2013.08.027.

Wang, Y., S. Hou, M. Ding, and W. Sun, 2020: On the performance of twentieth century reanalysis products for Antarctic snow accumulation. *Climate Dyn.*, **54**, 435–455, https://doi.org/10.1007/s00382-019-05008-4.

Xin, Y., Y. Dai, J. Li, X. Rong, and G. Zhang, 2019: Coupling the common land model to ECHAM5 atmospheric general circulation model. *J. Meteor. Res.*, **33**, 251–263, https://doi.org/10.1007/s13351-019-8117-y.

Zhang, H., F. Zhang, G. Zhang, Y. Ma, K. Yang, and M. Ye, 2018: Daily air temperature estimation on glacier surfaces in the Tibetan Plateau using MODIS LST data. *J. Glaciol.*, **64**, 132–147, https://doi.org/10.1017/jog.2018.6.

Zhang, Y., Y. Wang, and S. Hou, 2022: Reliability of Antarctic air temperature changes from Polar WRF: A comparison with observations and MAR outputs. *Atmos. Res.*, **266**, 105967, https://doi.org/10.1016/j.atmosres.2021.105967.